Application of imaging techniques for the characterization of lumps behaviour in gas–solid fluidized-bed reactors

Matteo Errigo, Alex Sebastiani, Stefano Iannello, Massimiliano Materazzi, Paola Lettieri [*]

Department of Chemical Engineering, University College London Gower St, London, United Kingdom

ABSTRACT

Gas-solid fluidized-bed reactors are often used in waste pyrolysis and gasification processes thanks to their excellent mixing properties, which guarantee temperature uniformity. However, this latter property can fail when large objects, such as lumps, are introduced or form in the system. Understanding the motion characteristics and thermal behaviour of lumps in a high temperature fluidized-bed reactor can help determining how the presence of lumps impact reactors' performance. This was the object of this study. In particular, this work aims to assess how process variables and physical properties impact the segregation behaviour, dispersion coefficients and heat transfer coefficients of these lumps during operation. The system used in this work is a down-scaled pseudo-2D fluidized bed operated at ambient temperature and at fluidization velocities ranging between 1 U_{mf} and 10 U_{mf}. Rutile sand with four different mean particle sizes (60 μm, 100 μm, 153 μm and 215 μm) was used as bed material. Fabricated lumps were introduced in the fluidized bed to reproduce realistic conditions, as when lumps form in a high-temperature fluid bed. The density ratio between the lump and the bed material particle was varied between 0.32 and 0.55 to account for different lump compositions. X-ray digital radiography and infrared thermography were used respectively to track the fabricated lumps and to obtain their temperature time evolution. The lump density was found not to have a significant effect on the lump dispersion coefficients or on the heat transfer coefficient. Optimal values of fluidization velocities that guarantee proper lump mixing and maximum heat transfer coefficient were obtained. This latter increases by up to 10 times if the optimal fluidization velocity is selected. An increase in the bed material particle size was found to cause an increase in the dispersion coefficients and a decrease in the heat transfer coefficient. The trend of the heat transfer coefficient as a function of the fluidization velocity was found to vary significantly between different bed material particle sizes. A new correlation for the Nusselt number as a function of the object Reynolds number and of the size ratio between lump and bed material was obtained. This correlation applies to cases where particle convection is the dominant mechanism of heat transfer. The results of this work provide important knowledge to minimize the impact of lumps on fluidized-bed reactors and to optimize their operation.

1. Introduction

Gas-solid fluidized-bed reactors are commonly used for the thermochemical treatment of waste feedstock thanks to the excellent contacting between solids and gas, ease of temperature control and feedstock flexibility that these reactors provide. These characteristics are enabled by the continuous and efficient mixing taking place in such reactors, allowing for excellent mass and heat transfer [1,2]. These, in turn, guarantee a better tolerance to inorganic matter, such as ashes, which tend to accumulate during treatment of non-conventional feedstock, such as biomass and waste-derived fuels [3]. However, the common

assumption that fluidized-bed reactors can be considered homogeneous in terms of concentration and temperature distributions can fail when larger objects, either externally introduced or internally formed, are present. These, in fact, can induce agglomeration, segregation and formation of undesirable by-products and disruption of normal operation [4]. The presence of these larger objects, in the form of fuel particles or lumps, is common in most of recent applications of high temperature fluidized-bed reactors. Some instances of such applications are plastic and biomass waste processing [5,6], nuclear spent fuel reprocessing [7] and chemical looping combustion [8]. Plastic waste, for example, is fed to fluidized-bed pyrolysers and gasifiers, usually together with inorganic materials such as ashes, where it softens and causes incipient

---

Nomenclature

Symbols

A [m^2]	Surface area
c [J/kg K]	Specific heat
D [m]	Bed diameter
D_x [m^2/s]	Lateral dispersion coefficient
D_y [m^2/s]	Vertical dispersion coefficient
d [m]	Particle diameter
Fr	Froude number
H_{bed} [m]	Fluidized bed height
h [W/m^2K]	Heat transfer coefficient
h^* [W/m^2K]	Apparent heat transfer coefficient
m [kg]	Mass
Nu^* [-]	Apparent Nusselt number
P [Pa]	Pressure
Re [-]	Reynolds number
T [K]	Temperature
t [s]	Time
U [m/s]	Superficial velocity
v [m/s]	Particle velocity
x [m]	Horizontal position in the bed
y [m]	Vertical position in the bed

Greek letters

Δ	Variation
ε [-]	Emissivity
μ [Pa s]	Dynamic viscosity
ρ [kg/m^3]	Density
ϕ [-]	Sphericity

Subscripts

0	Initial
avg	Average
$distr$	Distributor
em	Emulsion
g	gas
i	Instantaneous
$mean$	Mean value
mf	Minimum fluidization
obj	Immersed object
p	Bed material particle
PE	Polyethylene
PET	Polyethylene terephthalate
PP	Polypropylene
$sand$	Rutile sand
wb	Windbox
x	Horizontal
y	Vertical

---

agglomeration with bed material particles. This often leads to the formation of lumps with relatively long devolatilization times, in the order of magnitude of 1–3 min [6], which impair heat transfer and chemical reactions [5]. If the number of agglomerates in the reactor at a given time becomes excessive, defluidization of the reactor may occur, causing, in turn, an unplanned shutdown and economical losses. Ideally, the formation of lumps in fluidized-bed reactors should be avoided. However, this is not always possible, and the impact of such lumps on the reactor operation should be minimized. For this reason, a thorough understanding of the motion behaviour and of the heat transfer properties of these lumps is fundamental for an optimal process control limiting the segregation of lumps and maximizing their heat transfer in industrial fluidized-bed reactors.

From a hydrodynamic perspective, a lump can be described as an immersed object in the fluidized-bed system. Several studies were performed on the motion of immersed objects in gas–solid fluidized-bed reactors in terms of axial and lateral dispersion coefficients. The approaches used range from fully experimental [9–14], to fully simulative [15,16], or a mix of the two [17]. However, a systematic characterization of both vertical and lateral dispersion coefficients across the bubbling and slugging regimes during normal operating conditions is missing. Furthermore, dispersion coefficients are not sufficient to fully characterize the motion of immersed objects in a fluidized bed, as they do not provide information about the segregation or mixing tendency of the immersed object. A good vertical mixing of an immersed object allows for an enhanced bed-to-object heat transfer [18] good contact between volatiles and catalytic materials [19], and flameless reactions [2]. This helps in preventing the formation of hotspots, which are also cause of lumps and agglomerates formation. Previous studies investigated the mixing and segregation tendencies of immersed objects in fluidized-bed reactors [11,20–24], focussing on different segregation behaviours taking place in the different phases and on circulation patterns. The motion characteristics of lumps also determine how they affect the temperature distribution across the fluidized-bed reactor. Achieving a thorough understanding of the heat transfer between the fluidized bed and a single lump and of its dependence on the lump motion is important. While extensive (and rather historical) research was performed on the heat transfer between a fluidized bed and a fixed surface [25–31],

fewer studies were performed on the quantification of the more complex bed-to-freely moving object heat transfer coefficient. The main difference lies in the fact that the only significant contribution to heat transfer from the bubbles in the case of a freely moving object is indirect through mixing [32]. More recent studies started investigating the heat transfer coefficient between a fluidized bed and a larger immersed object [32–37], at varying particle size and fluidization regime. This case can be representative of a large agglomerate moving in and exchanging heat with a fluidized bed. These studies found the bed-to-immersed object heat transfer coefficient to slightly increase with the temperature of the bed, to slightly decrease with the immersed object size and, most importantly, to significantly decrease with an increase in the bed material particle size. To the authors' best knowledge there are no studies on the effect of the immersed object density on its heat transfer coefficient. As the object density plays an important role in the object motion, it might also have an indirect effect on its heat transfer coefficient with the fluidized bed. The bubble fraction, and consequently the mixing, in fact, vary with the position of the object in the fluidized bed. This means that also the relative motion between emulsion and object is indirectly affected by the object density. Furthermore, correlations to calculate the Nusselt number are available in the literature for the case when gas convection is the dominant heat transfer mechanism [38–41]. On the other hand, correlations for the Nusselt number have not been obtained for when the heat transfer is dominated by particle convection, which corresponds to the case with smaller bed material particles.

This work applies advanced imaging techniques, x-ray digital radiography and infrared thermography, to characterize the motion, in terms of segregation behaviour and dispersion coefficients, and the heat transfer of a fabricated lump in a fluidized-bed reactor treating plastic waste. The results obtained with the two techniques were then combined in order to show the link between the motion characteristics and the heat transfer of a lump in a fluidized-bed reactor. This study, for the first time, assesses the dependence of these characteristics on a wide range of fluidization velocities, going from minimum fluidization up to slugging regime. The role played by the lump density, both on the motion characteristics and on the heat transfer between lumps and fluidized beds, is also investigated. Furthermore, as far as the authors are aware, the effect of the particle size of the bed material on the dispersion

coefficients of an immersed object in a fluidized bed has never been investigated; this is also addressed in this work. Finally, a relationship between the lump motion characteristics and its heat transfer coefficient with the fluidized bed can be obtained for cases where the particle convection is the dominant mechanism of heat transfer.

2. Materials and methods

2.1. Experimental setup

The experimental setup is hereby described with a focus on the fluidized bed, on the fabricated lumps and on the imaging systems used.

2.1.1. Fluidized bed

The experimental setup used for the collection of data consists of a flat pseudo-2D fluidized bed with 1 cm-thick walls made of polymethyl methacrylate (Fig. 1). The pseudo-2D configuration was chosen in order to be able to measure the infrared radiation emitted by the fabricated lump directly. The dimensions of the column are 1000 mm × 100 mm × 10 mm and the distributor plate is a stainless steel sintered porous plate that guarantees even distribution of the fluidizing agent. Below the porous plate, a windbox containing ceramic beads (8–9 mm in diameter) pre-homogenizes the flow of fluid. The pressure drops across the windbox and the distributor plate are described by the following equation:

$$\Delta P_{wb+distr} = 21500 \bullet U^2 + 12000 \bullet U \tag{1}$$

where ΔP are the pressure drops in Pa and U is the superficial velocity through the windbox. These pressure drops across were found to satisfy the criteria for an even distribution of the gas across the distributor plate [24] and, therefore, a homogeneous fluidization across the bed cross section. This was further validated through visual check performed on the x-ray images.

The fluidized particles are high density (3000 kg/m^3) rutile sand, and the fluidizing agent is air at ambient temperature and pressure. Four different particle size ranges were used to study the effect of the particle size on the quantities studied. The minimum fluidization velocity, U$_{mf}$, corresponding to the different particle sizes used was experimentally determined through fluidization curves and the values are reported in Table 1 together with the bed material particle mean diameters.

The particle diameters used were carefully chosen to be at least 40 times smaller than the bed thickness. This is reported to be the suitable threshold value to have a 3D flow in a pseudo-2D fluidized bed [42], minimizing the interference of the wall effects with the solids circulation [43].

The conditions were chosen to maintain a similarity in hydrodynamic behaviour with a high temperature fluidized sand bed industrial reactor as per the Glicksman's scaling rules [44]. The industrial reactor would operate at near atmospheric pressure and temperature range between 650 and 850 °C, which are typical conditions for pyrolysis or gasification industrial processes, where plastic waste is used as a feedstock. Since all conditions simulated fall within the viscous limit (Re$_p$ < 4) [45], the only independent parameters to match according to Glicksman's scaling rules are $\frac{\rho_p U d_p^2}{\mu D}$, $\frac{gD}{U^2}$, D/H_{bed} and ϕ [44]. Table 2 shows the values of these parameters in industrial and scaled-down settings for the largest particle size. Further information regarding all particle sizes is reported in the supplementary material. The reference industrial fluidized-bed reactor was assumed to have internal diameter of 1 m. The diameter-to-bed height ratio can take a very wide range of values in industrial applications, going from 0.17 up to 3 [16,46–49]. For this study, the value 0.75 was considered.

2.1.2. Fabricated lump samples

Lumps were reproduced by the means of pumice beads with diameter equal to approximately 9 mm and with varying density. Different values of density allow to study the behaviour of lumps for different

Table 1
Mean particle diameters and minimum fluidization velocities of the rutile sand used in the experiments.

Mean particle diameter	Minimum fluidization velocity
60 μm	0.65 cm/s
100 μm	1.5 cm/s
153 μm	2.6 cm/s
215 μm	4.2 cm/s
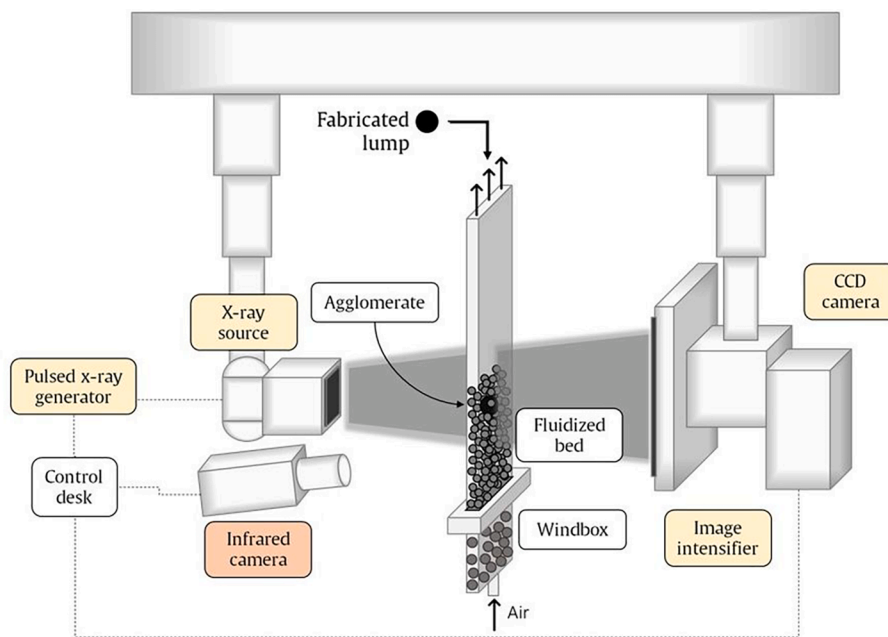
Fig. 1. Experimental setup: flat pseudo-2D fluidized bed with x-ray imaging system (yellow labels) and infrared camera for thermal imaging (orange label). (For interpretation of the references to colour in this figure legend, the reader is referred to the web version of this article.)

Table 2

Summary of the physical properties and operating conditions of the reference industrial fluidized-bed reactor and of the scaled-down fluidized bed.

	Industrial reactor	Scaled-down fluidized bed
Temperature T	750 °C	20 °C
Pressure P	1 atm	1 atm
Bed material particle density ρ_p	2650 kg/m³	3000 kg/m³
Minimum fluidization velocity U_{mf}	0.140 m/s	0.042 m/s
Bed material mean diameter d_p	625 μm	215 μm
Gas viscosity μ	4.58·10⁻⁵ Pa s	1.83·10⁻⁵ Pa s
Bed diameter D	1 m	0.1 m
$\frac{\rho_p U_{mf} d_p^2}{\mu_g D}$	3.2	3.2
$\frac{1}{Fr} = \frac{gD}{U_{mf}^2}$	501	550
D/H_{bed}	0.75	0.75
ϕ	0.86 [25]	0.86 [25]

compositions. The ratio between the lump size and the sand particle average size is approximately 40, allowing to consider the former as a freely moving object. This ratio corresponds to a lump size of 15 mm in the industrial reactor, which is in line with previous studies [6,46].

The change in density was achieved by loading different amounts of iron inside each sample (see Fig. 2a). Fig. 2b shows an x-ray image of one of the samples. Pumice was the sample material chosen because it can withstand high temperatures without degradation, it has a low density, and it presents a thermal conductivity (0.13–0.17 W/mK [50]) that perfectly matches that of plastics (0.11–0.22 W/mK [51]). This allows to account for the conductive heat transfer through the lump in a way that is representative of industrial applications. Iron filings were used as a tracer for x-ray imaging, and, at the same time, allowed to achieve the required lump densities. These fabricated lumps were heated up in a muffle furnace and then introduced from the top into the fluidized bed, operated at ambient temperature. For the sake of accuracy, the pumice beads were covered in matt black paint in order to bring their emissivity very close to 1, allowing for the black body approximation, and, therefore, having an infrared camera reading that can be directly linked to their temperature. The potential effect of this procedure on the heat transfer between the fabricated lumps and the fluidized bed is negligible, as it only affects the radiative heat transfer contribution, which is negligible for temperatures below 600 °C [52].

The devolatilization time for plastic particles with diameter ranging from 8 mm to 12 mm in a fluidized-bed reactor operated at temperatures between 500 °C and 650 °C was previously studied [6]. This was found to have values in the 40 s – 174 s range. Hence, due to the slow devolatilization of plastic-sand lumps, the formation of endogenous bubbles in plastic processing fluidized-bed reactors is limited and does not affect significantly the motion characteristics and heat transfer of the lump.
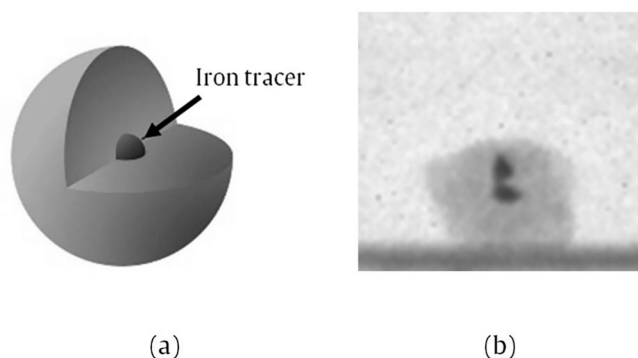
Fig. 2. Pumice beads samples: (a) schematic of the samples used, (b) x-ray image of one of the samples.

For this reason, the use of inert pumice as material to simulate lumps is justified. Contrarily, if biomass particles were to be studied, the release of volatiles bubbles would need to be taken into account as it would strongly affect the particle motion [6,53].

Depending on the amount of sand embedded in a plastic-sand lump, the lump density will vary. This was taken into account by using fabricated lumps with varying densities. The density ratios between the samples and the bed material particles, reported in Table 3, were used to draw a similarity with lumps in industrial applications. The sample density ratios allow to simulate the behaviour of lumps with densities ranging from that of pelletized plastic waste ($\rho_{PP,avg} \sim \rho_{PE,avg} \sim 900$ kg/m³, $\rho_{PET,avg} \sim 1300$ kg/m³) to that of polypropylene or polyethylene lumps with sand volume fraction of 30%. The density ratios of these two extremes in relation to silica sand ($\rho_{sand} \sim 2650$ kg/m³) are, in fact, and 0.34 and 0.54 respectively. The whole range between these two values is covered with the samples used.

2.1.3. Imaging systems

Fig. 1 shows the x-ray imaging system and the infrared camera, respectively with yellow and orange labels. The x-ray imaging system has been custom built by Shawcor and Genvolt. It is constituted of a pulsed high-voltage generator and an x-ray source, that together produce an x-ray beam; this is attenuated as it passes through the fluidized bed and then amplified and converted into a digital signal with an image intensifier and a CCD (charge-coupled device) camera. The system allows for image capture at a rate of up to 36 fps with a resolution of 1024 × 1040 pixels. On the other hand, the infrared camera is a short-wave infrared (SWIR) FLIR A6260 camera, allowing for imaging of the infrared radiation in the 0.9–1.7 um range. The integration time used during this study was 0.1 ms, which allowed to achieve 204 frames per second with a resolution of 640 × 512 pixels.

2.2. Methodology

Two techniques, x-ray digital radiography and infrared thermography (Fig. 3(b-c)), were used for the investigation of the motion and thermal behaviour of large particles in a fluidized bed. For both the techniques, the duration of the data sampling was of 30 s. Out of the corresponding frames, only the relevant ones were used for post-processing. Namely, for the x-ray particle tracking, only the frames corresponding to the duration of the transient for the particle to sink at the bottom or float at the top were used. On the other hand, for the infrared imaging data, only the initial frames with readings above the background noise level were considered.

2.2.1. X-ray digital radiography

X-ray digital radiography takes advantage of the penetrating power of × rays to create a 2D projection of a 3D object, where each pixel gives an indication of the attenuation the x-ray beam has gone through along a specific path. Although highly penetrating, x rays will undergo attenuation, which is a reduction in the x-ray beam intensity, due to the interaction phenomena of scattering, photoelectric absorption and pair production [54]. A great advantage of this diagnostic technique, just like infrared thermography, is that it is non-intrusive, meaning that it does not perturbate the normal operation of the fluidized bed, as other techniques might do. In this study, the x-ray attenuation is used to track the fabricated lump within the bed.

Table 3

Fabricated lump samples and relative densities.

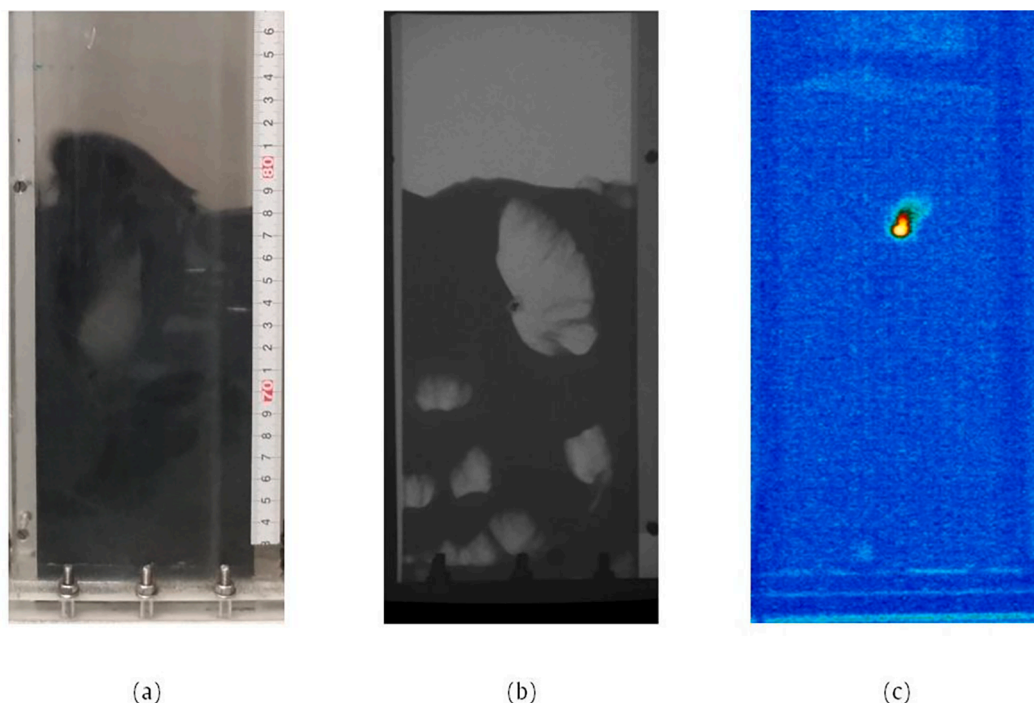| Sample number	ρ_{obj} [kg/m³]	ρ_{obj}/ρ_p [-]
1	970	0.32
2	1190	0.40
3	1410	0.47
4	1640	0.55

Fig. 3. Visual image (a), x-ray image (b) and thermal image (c) of the fluidized bed with a fabricated lump.

2.2.2. Infrared thermography

Infrared thermography is based on the emission of thermal radiation by all bodies at a temperature higher than 0 K. Most of the emitted thermal radiation falls in the infrared range of the electromagnetic spectrum. By collecting this radiation, information can be obtained on the temperature of the objects that are being observed. For this purpose, black bodies, or perfect emitters, are the best option. Their emissivity, ε, is equal to 1, meaning that they do not reflect infrared radiation. Instead, the totality of the radiation coming from them is emitted by the black bodies themselves. This allows to draw a direct correspondence between the infrared radiation collected by the camera and the body's temperature [55].

A calibration curve was obtained in order to convert the reading from the infrared camera into the temperature of the object that emitted the infrared radiation. More details about the calibration procedure are reported in the supplementary material.

To study the thermal behaviour of the fabricated lumps, these were heated up in a muffle furnace up to approximately 550 °C and then dropped inside the fluidized bed at ambient temperature, while the infrared camera recorded their infrared emission. The initial temperature of the fabricated lump was chosen to reproduce the same temperature gradient that would be observed by a plastic-sand agglomerate in a hot fluidized bed during thermochemical conversion [56]. The present study is carried out under the assumption that the heat transfer coefficient between a cold immersed object and a hot fluidized bed is the same as the one between a hot object and a cold bed under forced convection. This assumption is widely adopted in the literature [48].

3. Results and discussion

Experiments were carried out varying the lump density, the fluidization velocity and the bed material particle size.

3.1. Motion characteristics of the lumps via x-ray digital radiography

X-ray digital radiography was used to track the fabricated lump moving within the fluidized bed. Some typical x-ray images for different gas superficial velocities are shown in Fig. 4.

By identifying the lump and keeping track of its position inside the bed, a trajectory can be obtained and plotted as a function of time. This is shown in Fig. 5(a), where each circle corresponds to one position. The time is shown with the circle colour, going from blue to green as time goes by. Fig. 5 (b), on the other hand, shows the time evolution of the vertical position of the fabricated lump only. The dashed lines in both figures represent the levels between which the fluidized bed interface oscillates due to the eruption of gas bubbles at the surface.

A systematic approach was then adopted to observe the effects of the lump density, of the gas superficial velocity and of the bed material particle size. The plots for the most significant values of fluidization number are reported in Fig. 6, which shows the time evolution of the vertical position of the fabricated lump for different lump densities and gas superficial velocities.

3.1.1. Segregation behaviour of lumps

Table 4 summarizes the behaviour of the fabricated lumps for different values of fluidization velocity and lump-to-particle density ratio. These results were obtained for the largest particle size ($d_{p,mean}$ = 215 µm).

Two different trends were observed: for superficial velocities smaller than or equal to 2 U_{mf}, by increasing the density of the fabricated lump, segregation towards the bottom of the reactor increases. On the other hand, when the gas superficial velocity increases beyond 4 U_{mf}, mixing within the fluidized bed becomes so vigorous that the effect of the lump density becomes less relevant. Industrial bubbling fluidized-bed reactors are usually operated at several times the minimum fluidization velocity [57]. However, the gas superficial velocity guaranteeing the proper mixing of lumps (between 2 U_{mf} and 4 U_{mf} in this case) is expected to vary with the operating conditions and the physical properties of the
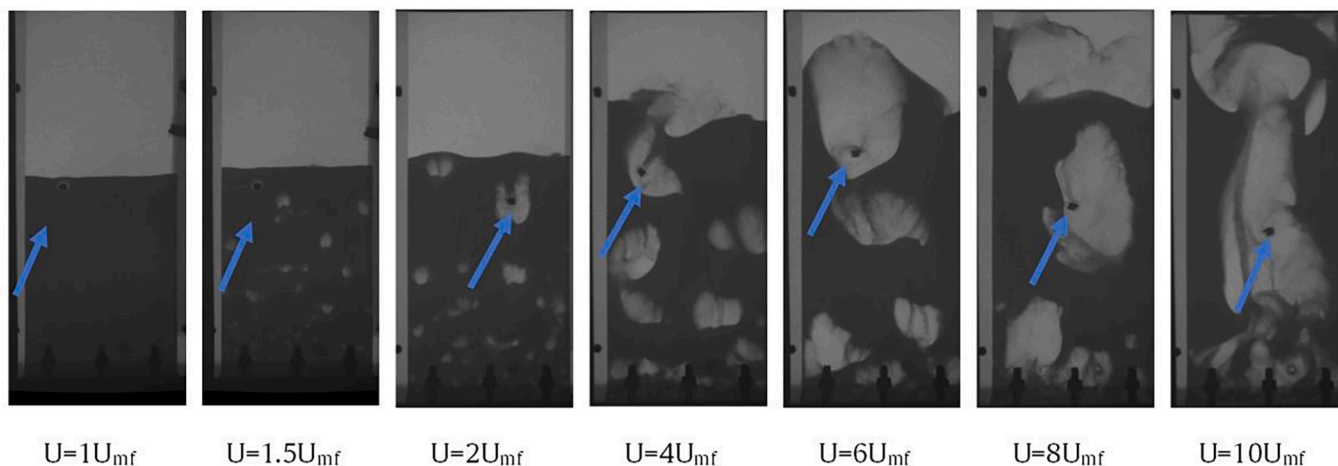
Fig. 4. X-ray images of the pseudo-2D fluidized bed for different gas superficial velocities (sample 4, $d_{p,mean}$ = 215 μm).
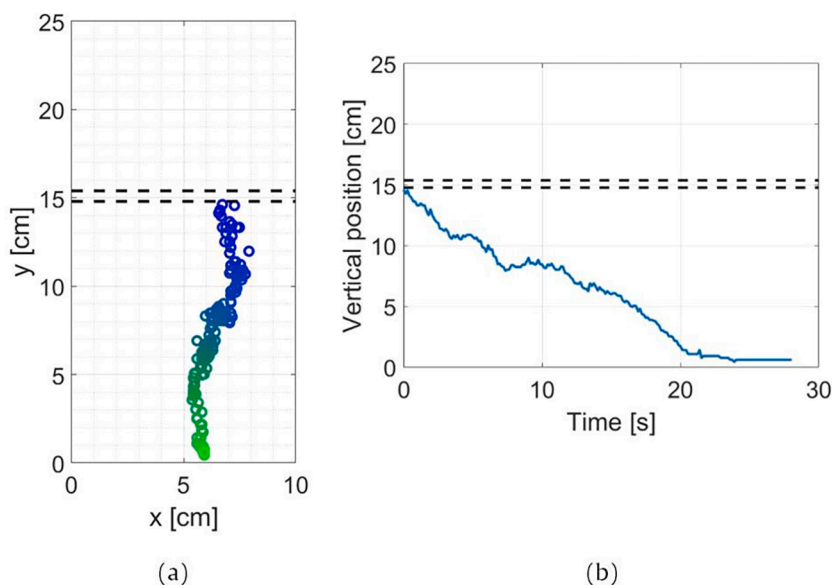

(a)   (b)

Fig. 5. Example of x-ray digital radiography data for sample 4 at 2 U_{mf} and with $d_{p,mean}$ = 215 μm: (a) trajectory of the fabricated lump (going from blue to green) and (b) time evolution of the lump vertical position. (For interpretation of the references to colour in this figure legend, the reader is referred to the web version of this article.)

system. Attention needs to be paid in identifying this value, to then operate the fluidized-bed reactor at larger fluidization velocities in order to avoid the segregation of lumps. On the other hand, too large fluidization velocities could bring about operational problems, such as attrition and elutriation of fines, which would be detrimental for the reactor operation. A good balance between these two mechanisms needs to be found in the design phase of a fluidized-bed reactor.

The effect of the bed material particle size was then investigated for sample 1. The results are summarized in Table 5 and show how increasing the bed material particle size, while keeping the fluidization number constant, improves the mixing of the lump within the fluidized bed. This can be attributed to larger minimum fluidization velocities corresponding to larger particle sizes.

3.1.2. Vertical and lateral dispersion coefficients of lumps

The vertical and lateral motion of the fabricated lump was studied in terms of vertical and lateral dispersion coefficients, defined as follows:

$$D_y = \frac{(\Delta y_i)^2}{2\Delta t} \tag{2}$$

$$D_x = \frac{(\Delta x_i)^2}{2\Delta t} \tag{3}$$

For the calculation of the dispersion coefficients, the time step Δt was kept constant and equal to 1/36 s, and the horizontal and vertical displacements, Δx and Δy respectively, were evaluated over this constant time step. The minimum time scale for the gulf streams was estimated to be around 1 s. Hence, a sampling frequency of 36 Hz was deemed appropriate to describe the phenomenon studied.

The experiments were first carried out with the largest particle size ($d_{p,mean}$ = 215 μm) for different lump densities and fluidization velocities, and the results are reported in Fig. 7. They show a very clear correlation between the dispersion coefficients and the fluidization number U/U_{mf}. The lump density does not seem to affect the dispersion coefficients as there is no clear trend pointing towards a larger or smaller dispersion coefficients as the lump density increases. For low fluidization numbers, this is attributable to the fact that the movement of the fabricated lump, even for large densities, is very slow. On the other hand, for large fluidization numbers, the effect of the vigorous mixing appears to overcome the effect of the density, as shown in Fig. 6(b).
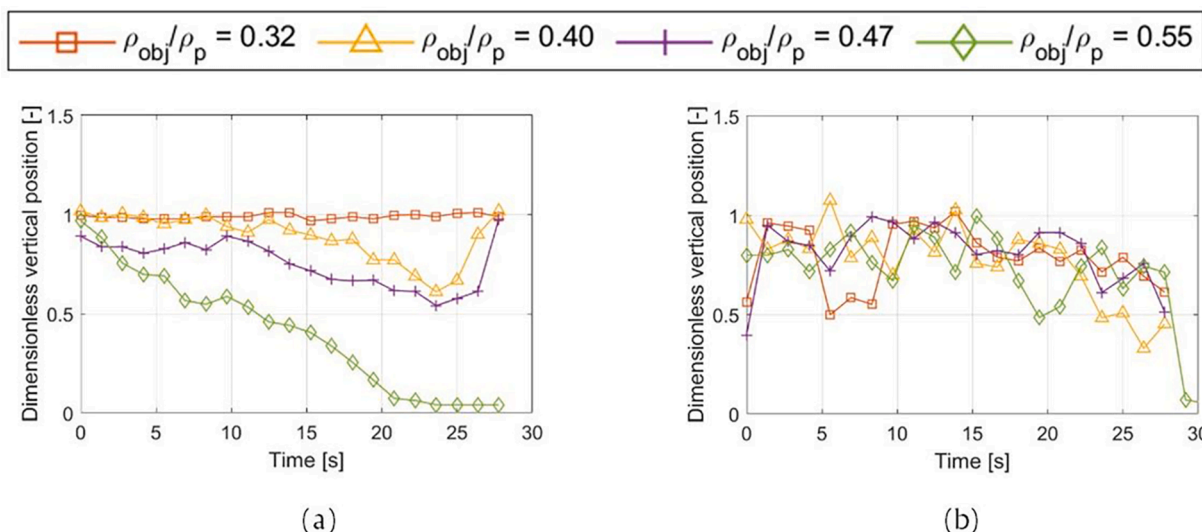
Fig. 6. Time evolution of the vertical position of the fabricated lumps in the fluidized bed ($d_{p,mean}$ = 215 μm) for (a) 2 U_{mf} and (b) 4 U_{mf}.

Table 4
Behaviour of the fabricated lumps for different values of fluidization velocity and lump-to-particle density ratio ($d_{p,mean}$ = 215 μm).

	U_{mf}	1.5 U_{mf}	2 U_{mf}	4 U_{mf}	6 U_{mf}	8 U_{mf}	10 U_{mf}
ρ_{obj}/ρ_p = 0.32	Float	Float	Float	Mixed	Mixed	Mixed	Mixed
ρ_{obj}/ρ_p = 0.40	Float	Float	Mixed	Mixed	Mixed	Mixed	Mixed
ρ_{obj}/ρ_p = 0.47	Float	Float	Mixed	Mixed	Mixed	Mixed	Mixed
ρ_{obj}/ρ_p = 0.55	Sink	Sink	Sink	Mixed	Mixed	Mixed	Mixed

Table 5
Behaviour of the fabricated lumps for different values of fluidization velocity and bed material particle size (ρ_{obj}/ρ_p = 0.32).

	U_{mf}	1.5 U_{mf}	2 U_{mf}	4 U_{mf}	6 U_{mf}	8 U_{mf}	10 U_{mf}
$d_{p,mean}$ = 60 μm	Float	Float	Float	Float	Float	Mixed	Mixed
$d_{p,mean}$ = 100 μm	Float	Float	Float	Float	Mixed	Mixed	Mixed
$d_{p,mean}$ = 153 μm	Float	Float	Float	Mixed	Mixed	Mixed	Mixed
$d_{p,mean}$ = 215 μm	Float	Float	Float	Mixed	Mixed	Mixed	Mixed

However, dispersion coefficients are not sufficient to fully characterize the motion of lumps as they only give an indication of the average motion in a time interval. For example, referring to the 2 U_{mf} column in Table 4, even though the vertical dispersion coefficient for different lump densities is very similar, the tendency of the lump to sink, mix or float varies greatly with its density. Furthermore, by definition, dispersion coefficients are used to characterize the motion of particles evolving towards a homogeneous distribution. This means that, for the experimental runs in which the lump sank or floated, the vertical dispersion coefficient is not to be interpreted from a physical point of view, but rather as a measure of the average motion of such lumps. However, as can be observed in Fig. 7, the trend of the vertical dispersion coefficient is continuous for different segregation behaviours. This is particularly true for the experiments run at 2 U_{mf}, where, although completely different segregation behaviours can be observed for different lump densities (Table 4), the vertical dispersion coefficient is constant. On the other hand, the lateral dispersion coefficient for the experimental runs at larger flow rates is also to be interpreted as an indication of the average lateral motion of lumps rather than by its physical definition. In these cases, in fact, a single bubble path is present, and dispersion between different mixing cells is not possible. A mixing cell is defined as the volume comprising a bubble path and the flow structure around it [4]. This concept has been applied to study the lateral dispersion of fuel particles in wide fluidized beds [16,58].

Results were then compared to previous results found in the literature, showing good qualitative agreement, although quantitative comparison is complicated. The numeric values, in fact, are highly dependent not only on the bed material and lump physical properties, but also on the fluidized-bed cross section [58]. For example, a study [10] showed the values of the lateral dispersion coefficient for fluidization numbers of 6, 8 and 11 and found them to be 5 to 15 times larger than the ones found in this study. The experimental setup in [10], however, is supposed to represent the behaviour of a significantly larger fluidized bed (0.85 m × 0.85 m) than the one used in this study. Very good agreement is found with Monte Carlo modelling results [59] in terms of lateral dispersion coefficient. These also show a power law behaviour that seems to emerge from Fig. 7.

Once established that the density does not affect the vertical and lateral dispersion coefficients, the effect of the bed material particle size on the dispersion coefficients was assessed for the fabricated lump number 1 (ρ_{obj}/ρ_p = 0.32). Four different particle sizes were used (refer back to Table 1) and Fig. 8 shows the results. A power law behaviour with respect to the fluidization velocity can again be observed. Furthermore, the bed material particle size also clearly has an impact on the value of the dispersion coefficients.

Fig. 9 shows the dependence of the dispersion coefficients on the bed material particle mean diameter for different fluidization numbers, and, also in this case, the relationship seems to approach a power law. Some discrepancies from this trend can be observed both in Fig. 8 and in Fig. 9 for the lateral dispersion coefficients. This is likely due to to experimental error and to the time scale the experiments were carried out on.

This increase in dispersion coefficients with the bed material particle size can be attributed to larger minimum fluidization velocities for larger bed material particles, as well as to a more vigorous bubbling, even slugging at times, and therefore enhanced mixing.

The immersed object density was found not to influence the vertical and the lateral dispersion coefficients. On the other hand, these
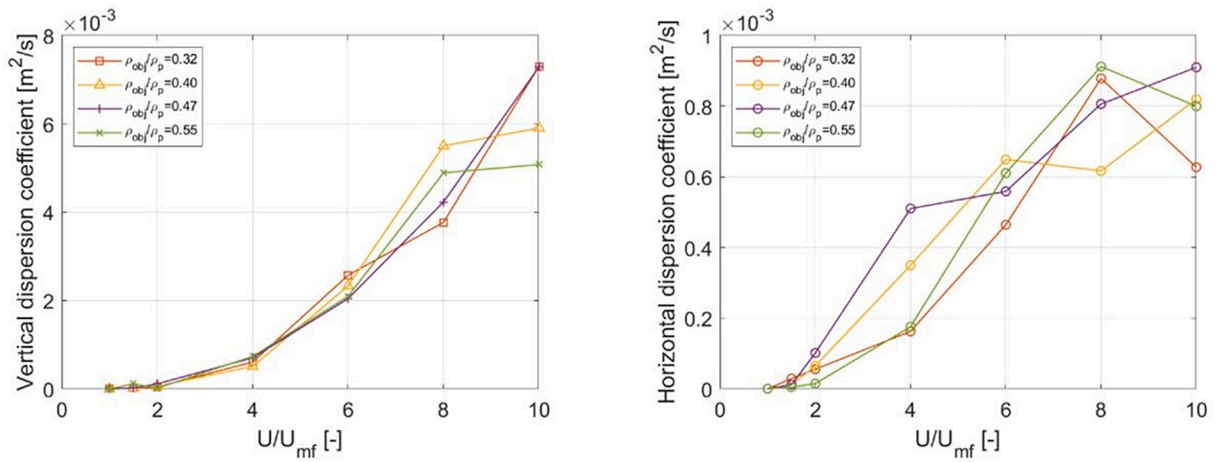
Fig. 7. Vertical and lateral dispersion coefficients of a fabricated lump versus fluidization number for different density ratios ($d_{p,mean} = 215$ μm).
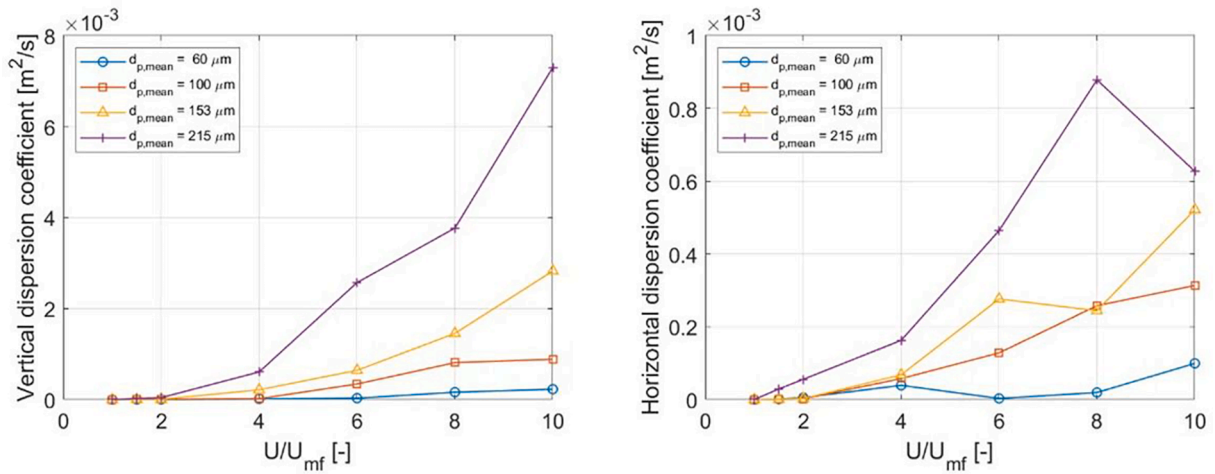

Fig. 8. Vertical and lateral dispersion coefficients of a fabricated lump versus fluidization number for different bed material particle sizes ($\rho_{obj}/\rho_p = 0.32$).
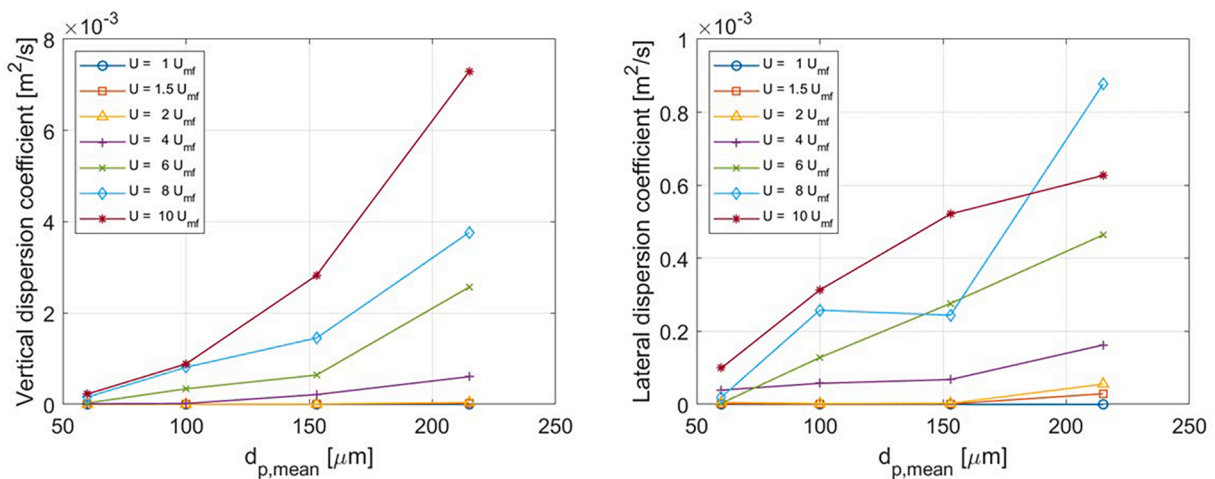

Fig. 9. Vertical and lateral dispersion coefficients of a fabricated lump versus bed material particle sizes for different fluidization numbers ($\rho_{obj}/\rho_p = 0.32$).

dispersion coefficients were found to be strongly affected by the fluidization velocity and by the bed material particle size. Both of these relationships show a power-law behaviour. In commercial applications of fluidized-bed reactors the formation of lumps should be avoided. However, this is not always possible, and, to minimize their impact on the operation of a fluidized-bed reactor, their segregation needs to be

prevented. This can be obtained either by operating the reactor at larger fluidization numbers or by increasing the bed material particle size.
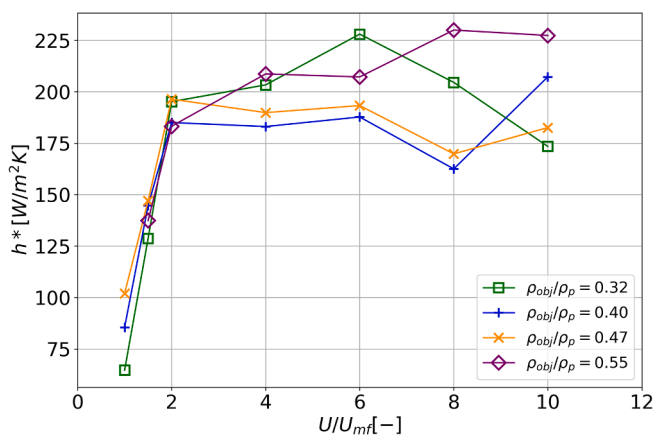
3.2. Heat transfer coefficient between fluidized bed and lumps via infrared thermography

The detailed procedure followed to obtain the heat transfer coefficient starting from the infrared camera is reported in the supplementary material. It consists in converting the infrared reading into a temperature evolution, which is then fitted with an exponential function, whose curvature provides the heat transfer coefficient. The obtained apparent heat transfer coefficient embeds the conductive heat transfer through the lump radius to make its application more immediate.

3.2.1. Effect of the lump density on the heat transfer coefficient

This procedure was first used to study the effect of the lump-to-bed material density ratio over the heat transfer coefficient. Fig. 10 shows the resulting values for the different samples and for different values of gas superficial velocity. These results were obtained for the largest particle size ($d_{p,mean} = 215$ μm), which belongs to group B in Geldart's classification.

For small superficial flow rates, the heat transfer coefficients increase fairly sharply (up to fourfold) with the superficial velocity from U_{mf} to $2U_{mf}$. By contrast, once $2\ U_{mf}$ has been reached, the heat transfer tends to stabilize and stay constant even for superficial velocities of up to 10 U_{mf}. Some discrepancies from this constant behaviour can be observed and are likely due to experimental error. It is worth noting that the infrared imaging technique for the measurement of the heat transfer coefficient seems to be more reliable at low fluidization numbers, as better consistency between different measurements is observed. This is probably due to a less vigorous mixing behaviour, which, in turn, allows for a slower transient. The immersed object density, once again, does not seem to play an important role in the results, as no particular pattern can be identified for varying densities. Since this bed material belongs to group B in Geldart's classification, the excess of fluidizing gas with respect to the minimum fluidization velocity results in the formation of bubbles, assuming that the emulsion voidage is constant, according to the two-phase model. This means that the gas superficial velocity in the emulsion is constant. Nevertheless, the heat transfer coefficient increases, pointing at the fact that the main mechanism of heat transfer must be particle convection. Comparison between the results reported in this study and literature data is complicated due to a different definition of the heat transfer coefficient h. The value used in this study, in fact, is a heat transfer coefficient that also takes into account the thermal conductivity resistance of the lump. For this reason, the resulting heat transfer coefficient is expected to be lower than the commonly used one.
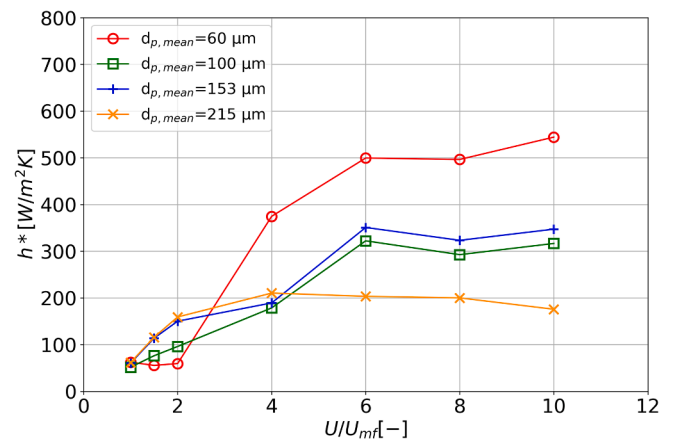
However, since the material used to simulate lumps presents a very similar thermal conductivity to that of plastic, the resulting value of apparent heat transfer coefficient would still be representative of thermochemical applications. To distinguish this apparent heat transfer coefficient from the most commonly used heat transfer coefficient, the former is referred to as h*. Qualitatively, the dependence of the heat transfer coefficient with the fluidization velocity agrees with previously published results, which found that the heat transfer coefficient increases with increasing the fluidization velocity up to a certain value, after which it becomes constant [37,60–62]. Other studies, however, found a maximum of the heat transfer coefficient for a specific value of fluidization velocity [32,63], which depended on the bed material particle size. Nevertheless, from a physical point of view, a maximum in the heat transfer coefficient is not expected. The dependence of the heat transfer coefficient on the fluidization velocity is dominated by two mechanisms. The first one consists in larger flow rates causing shorter residence times of emulsion packets near an immersed object, and, therefore, improving the heat transfer between object and fluidized bed. The second mechanism consists in an increasing fraction of bubbles in contact with the surface as the fluidization velocity increases, which worsens the heat transfer due to the poor thermal properties of gases [64]. While in the case of fixed surfaces, these two mechanisms are comparable, in the case of a freely moving object the contact time between immersed objects and bubbles is sufficiently small [60] that the blanketing phenomenon can be neglected. The heat transfer coefficient is then expected to increase asymptotically with the fluidization velocity.

In industrial settings the reactor needs to be operated at fluidization velocities larger than the minimum value guaranteeing a maximum heat transfer coefficient. At the same time, going too far beyond this value does not provide any advantage from a heat transfer point of view, and causes the intensification of some operational problems. The lump-to-bed material density ratio does not seem to be affecting the heat transfer coefficient, at least for the range of density ratios that was studied.

3.2.2. Effect of the bed material particle size on the heat transfer coefficient

The effect of the bed material particle mean diameter was studied for the fabricated lump number 1 ($\rho_{obj}/\rho_p = 0.32$). The results are reported in Fig. 11 and show how smaller particle sizes allow for larger heat transfer coefficients. Furthermore, a general trend can be identified: for all particle sizes the heat transfer coefficient increases almost linearly for a range of fluidization velocities, to then become approximately constant. The increase, however, shifts to larger fluidization numbers as the particle size decreases. The smaller bed material particles, in fact, belong to group A in the Geldart classification, meaning that the corresponding

Fig. 10. Heat transfer coefficient between bed and fabricated lump versus gas superficial velocity for different values of lump density ($d_{p,mean} = 215$ μm).

Fig. 11. Heat transfer coefficient between bed and fabricated lump versus superficial gas velocity for different values of bed material mean diameter ($\rho_{obj}/\rho_p = 0.32$).

fluidized bed tends to expand for a range of fluidization velocities before bubbles start forming. Therefore, for small particle sizes and low fluidization numbers, no bubbles are present, and, consequently, the mixing and the circulation patterns are less pronounced. This is clearly observable for the smallest particle size used, $d_{p,mean} = 60$ μm, where the heat transfer coefficient remains constant until the fluidization velocity exceeds $U = 2U_{mf}$. Again, this can be interpreted as further evidence that most of the heat transfer occurs between the lump and the bed material particles, as a sharp increase can be observed in correspondence of the start of the bubbling behaviour, while the voidage in the emulsion phase can be considered constant.

The increase of the heat transfer coefficient with smaller particle sizes agrees with previous studies [33,36,52,64] and can be attributed to a better contact between the lump and the bed material. However, it is the first time that the difference between group A and group B particles in the heat transfer coefficient trend is directly observed. In practical terms, Fig. 11 shows that if a group A bed material is used, a shift towards larger fluidization numbers is even more important to guarantee a maximum heat transfer coefficient. The minimum gas superficial velocity guaranteeing a maximum heat transfer coefficient, in fact, can be at fluidization velocities that are significantly larger than the minimum fluidization value (6 U_{mf} for bed material with $d_{p,mean} = 60$ μm).

3.2.3. Nusselt number correlation

An empirical correlation is obtained for the calculation of Nu* using the measured h* as a function of the Reynolds number, by fitting the experimental data with the commonly used semi-empirical correlation [40,41] of the type:

$$Nu^* = 2 + aRe_{obj}{}^b \left(d_{obj}/d_p \right)^e \tag{4}$$

which satisfies Nu* = 2 for stagnant gas and where a, b and e are fitting coefficients. While this type of correlation has mostly been used when the heat transfer is dominated by gas convection, it also fits satisfactorily the case studied, where particle convection is the main heat transfer mechanism. The size ratio, and therefore the contact, between the bed material and the lump has a major impact on the Nusselt number. On the other hand, the Prandtl number, used in previous studies on gas convection-dominated heat transfer [65,66], is not expected to impact the heat transfer significantly.

Fig. 12 shows the experimental points and the resulting fitting. The correlation obtained is:

$$Nu^* = 2 + 0.037Re_{obj}{}^{0.38} \left(d_{obj}/d_p \right)^{1.14} \tag{5}$$

where Re_{obj} is obtained from the x-ray images as it follows. The immersed object instantaneous velocity can be used to obtain a Reynolds number referred to the relative motion between the object and the gas in the emulsion phase, which is more representative than the commonly used Re_{obj} calculated using either the minimum fluidization superficial velocity [67] or the superficial gas velocity [68]. An instantaneous $Re_{obj, i}$ can be obtained according to Equation (6), and this is then averaged over time to obtain a mean value to use in Equation (5).

$$Re_{obj,i} = \frac{\rho_g \left| \overrightarrow{v_{obj,i}} - \overrightarrow{U_{em}} \right| d_{obj}}{\mu_g} \tag{6}$$

where ρ_{gas} and μ_{gas} are respectively the gas density and dynamic viscosity, v_{obj} is the object velocity, U_{em} the gas velocity in the emulsion phase, assumed to be constant and upwards. The subscript i indicates the instantaneous value of the quantity it is referred to. The advantage given by using this Re_{obj} over other definitions is that it takes into account the actual motion of the immersed object with respect to the emulsion.

The coefficients in Equation (5) are fairly different from the ones seen in the literature and this can be attributed to the different definitions of the Reynolds and of the Nusselt numbers with respect to previous studies. The first one, in fact, is referred to the relative motion between immersed object and gas in the emulsion phase, while the Nusselt number was obtained with h*, also taking the conduction of heat through the fabricated lump into account. Equation (5) can then be used to have an accurate prediction of the Nusselt number between a fluidized bed and a lump in industrial applications for a wide range of fluidization velocities and bed material particle sizes.

4. Conclusion

X-ray digital radiography and infrared thermography were used to characterize the segregation behaviour, the dispersion coefficients, and the heat transfer coefficient of a lump inside a fluidized-bed reactor. Wide ranges of fluidization velocities and particle sizes were investigated and showed power-law behaviours for dispersion coefficients with respect to both of these parameters. The dispersion coefficients were found to be in the 10^{-4} m/s^2 and 10^{-3} m/s^2 range for horizontal and vertical dispersion coefficients respectively. Optimal values of fluidization velocities preventing lump segregation and maximizing the heat transfer between the lump and the fluidized bed, increasing by a factor of up to 10, were found. These values vary significantly, from a minimum of 2 U_{mf} to a maximum of 8 U_{mf}, depending on the lump density and on the bed material particle size. The lump density was found not to significantly affect the dispersion coefficients or the heat transfer coefficient; however, it played a role in the propensity to cause segregation at the smaller fluidization velocities. An increase in the bed material particle size was shown to decrease the heat transfer coefficient, by up to a factor of 2.5, and to reduce the minimum fluidization number that guarantees full lump mixing. Finally, a combination of the data obtained with the two techniques allowed to draw a correlation for the Nusselt number as a function of the object Reynolds number and the object-to-bed material size ratio. This correlation is valid for cases where particle convection is the dominant heat transfer mechanism. An improved knowledge of the behaviour of agglomerates in fluidized-bed reactors can help in choosing design parameters and operating conditions minimizing the chances of operational problems.

CRediT authorship contribution statement

Matteo Errigo: Conceptualization, Formal analysis, Investigation, Methodology, Software, Visualization, Writing – original draft. **Alex Sebastiani:** Conceptualization, Investigation, Writing – review & editing. **Stefano Iannello:** Conceptualization, Writing – review & editing. **Massimiliano Materazzi:** Conceptualization, Writing – review & editing, Supervision. **Paola Lettieri:** Writing – review & editing, Supervision, Funding acquisition.
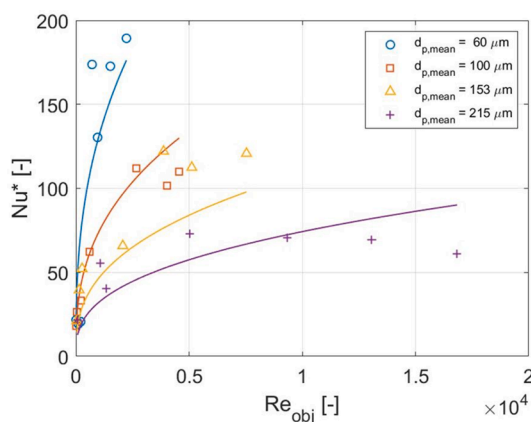

Fig. 12. Apparent Nusselt number plotted versus object Reynolds number for different bed material particle sizes: experimental data (points) and fitting (solid lines).

Declaration of Competing Interest

The authors declare that they have no known competing financial interests or personal relationships that could have appeared to influence the work reported in this paper.

Data availability

Data will be made available on request.

Appendix A. Supplementary data

Supplementary data to this article can be found online at https://doi.org/10.1016/j.fuel.2023.128634.

References

[1] L. G. Gibilaro, *Fluidization Dynamics*. Elsevier, 2001. doi: 10.1016/B978-0-7506-5003-8.X5000-9.
[2] J. G. Yates and P. Lettieri, Fluidized-Bed Reactors: Processes and Operating Conditions, vol. 26, no. 10. 2016.
[3] Iannello S, Morrin S, Materazzi M. Fluidised bed reactors for the thermochemical conversion of biomass and waste. Kona Powder Part J 2020;37(37):114–31. https://doi.org/10.14356/kona.2020016.
[4] Salatino P, Solimene R. Mixing and segregation in fluidized bed thermochemical conversion of biomass. Powder Technol 2017;316:29–40. https://doi.org/10.1016/j.powtec.2016.11.058.
[5] M. L. Mastellone and U. Arena, "Bed defluidisation during the fluidised bed pyrolysis of plastic waste mixtures," *Polym Degrad Stab*, vol. 85, no. 3 SPEC. ISS., pp. 1051–1058, 2004, doi: 10.1016/J.POLYMDEGRADSTAB.2003.04.002.
[6] Iannello S, Foscolo PU, Materazzi M. Investigation of single particle devolatilization in fluidized bed reactors by X-ray imaging techniques. Chem Eng J 2022;431:1385–8947. https://doi.org/10.1016/j.cej.2021.133807.
[7] L. G. Williams, *Reprocessing and Recycling of Spent Nuclear Fuel*, vol. 9. 2015.
[8] Kuusik R, Trikkel A, Lyngfelt A, Mattisson T. High temperature behavior of NiO-based oxygen carriers for Chemical Looping Combustion. Energy Procedia Feb. 2009;1(1):3885–92. https://doi.org/10.1016/J.EGYPRO.2009.02.191.
[9] Pallarès D, Johnsson F. A novel technique for particle tracking in cold 2-dimensional fluidized beds - Simulating fuel dispersion. Chem Eng Sci 2006;61(8):2710–20. https://doi.org/10.1016/j.ces.2005.11.030.
[10] Köhler A, Pallarès D, Johnsson F. Magnetic tracking of a fuel particle in a fluid-dynamically down-scaled fluidised bed. Fuel Process Technol 2017;162:147–56. https://doi.org/10.1016/j.fuproc.2017.03.018.
[11] Sette E, Berdugo Vilches T, Pallarès D, Johnsson F. Measuring fuel mixing under industrial fluidized-bed conditions - A camera-probe based fuel tracking system. Appl Energy 2016;163:304–12. https://doi.org/10.1016/j.apenergy.2015.11.024.
[12] Schlichthaerle P, Werther J. Solids mixing in the bottom zone of a circulating fluidized bed. Powder Technol 2001;120(1–2):21–33. https://doi.org/10.1016/S0032-5910(01)00342-4.
[13] Lundberg L, Soria-Verdugo A, Pallarès D, Johansson R, Thunman H. The role of fuel mixing on char conversion in a fluidized bed. Powder Technol 2017;316:677–86. https://doi.org/10.1016/j.powtec.2016.10.060.
[14] Sette E, Pallarès D, Johnsson F, Ahrentorp F, Ericsson A, Johansson C. Magnetic tracer-particle tracking in a fluid dynamically down-scaled bubbling fluidized bed. Fuel Process Technol 2015;138:368–77. https://doi.org/10.1016/j.fuproc.2015.06.016.
[15] Lian G, Zhong W, Liu X. CFD-DEM Investigation of Fuel Dispersion Behaviors in a 3D Fluidized Bed. Ind Eng Chem Res 2021;60(36):13272–85. https://doi.org/10.1021/acs.iecr.1c02443.
[16] Garcia-Gutierrez LM, Soria-Verdugo A, Ruiz-Rivas U. Optimization of the feeding ports location in a fluidized bed combustor based on Monte Carlo simulations of fuel particles motion. Fuel 2015;141:82–92. https://doi.org/10.1016/j.fuel.2014.10.027.
[17] Chirone R, Miccio F, Scala F. On the relevance of axial and transversal fuel segregation during the FB combustion of a biomass. Energy Fuel 2004;18(4):1108–17. https://doi.org/10.1021/ef034084j.
[18] Lundberg L, Tchoffor PA, Pallarès D, Johansson R, Thunman H, Davidsson K. Influence of surrounding conditions and fuel size on the gasification rate of biomass char in a fluidized bed. Fuel Process Technol Apr. 2016;144:323–33. https://doi.org/10.1016/J.FUPROC.2016.01.002.
[19] Sette E, Berdugo Vilches T, Pallarès D, Johnsson F. Measuring fuel mixing under industrial fluidized-bed conditions - A camera-probe based fuel tracking system. Appl Energy 2016;163:304–12. https://doi.org/10.1016/j.apenergy.2015.11.024.
[20] Fotovat F, Chaouki J, Bergthorson J. Distribution of large biomass particles in a sand-biomass fluidized bed: Experiments and modeling. AIChE J Mar. 2014;60(3):869–80. https://doi.org/10.1002/AIC.14337.
[21] Fotovat F, Chaouki J. Characterization of the upward motion of an object immersed in a bubbling fluidized bed of fine particles. Chem Eng J 2015;280:26–35. https://doi.org/10.1016/j.cej.2015.05.130.
[22] Soria-Verdugo A, Garcia-Gutierrez LM, Sanchez-Delgado S, Ruiz-Rivas U. Circulation of an object immersed in a bubbling fluidized bed. Chem Eng Sci 2011;66(1):78–87. https://doi.org/10.1016/j.ces.2010.10.006.
[23] Köhler A, Guío-Pérez DC, Prati A, Larcher M, Pallarès D. Rheological effects of a gas fluidized bed emulsion on falling and rising spheres. Powder Technol Nov. 2021;393:510–8. https://doi.org/10.1016/J.POWTEC.2021.07.064.
[24] Kunii D, Levenspiel O. Fluidization Engineering 1991;vol. 3, no. 1. https://doi.org/10.1016/0032-5910(69)80087-2.
[25] Mickley HS, Fairbanks DF. Mechanism of heat transfer to fluidized beds. AIChE J Sep. 1955;1(3):374–84. https://doi.org/10.1002/AIC.690010317.
[26] Botterill JSM. Heat transfer to gas-fluidized beds. Powder Technol 1970;4(1):19–26. https://doi.org/10.1016/0032-5910(70)80003-1.
[27] Kubie J, Broughton J. A model of heat transfer in gas fluidized beds. Int J Heat Mass Transf 1975;18(2):289–99. https://doi.org/10.1016/0017-9310(75)90160-X.
[28] Molerus O, Mattmann W. Heat Transfer Mechanisms in Gas Fluidized Beds Part 1. Maximum Heat Transfer Coefficients 1992.
[29] Wong YS, Seville JPK. Single-particle motion and heat transfer in fluidized beds. AIChE J 2006;52(12):4099–109. https://doi.org/10.1002/AIC.11012.
[30] Abdelmotalib HM, Ko DG, Im IT. A study on wall-to-bed heat transfer in a conical fluidized bed combustor. Appl Therm Eng 2016;99:928–37. https://doi.org/10.1016/j.applthermaleng.2016.01.054.
[31] Yates JG. In: Fundamentals of Fluidized Bed Chemical Processes. Elsevier; 1983. p. 4–71.
[32] Parmar MS, Hayhurst AN. The heat transfer coefficient for a freely moving sphere in a bubbling fluidised bed. Chem Eng Sci 2002;57(17):3485–94. https://doi.org/10.1016/S0009-2509(02)00259-2.
[33] Prins W, Maziarka P, De Smedt J, Ronsse F, Harmsen J, Van Swaaij WV. Heat transfer from an immersed fixed silver sphere to a gas fluidized bed of very small particles. Therm Sci 2019;23:S1425–33. https://doi.org/10.2298/TSCI180928175P.
[34] Garcia-Gutierrez LM, Hernández-Jiménez F, Cano-Pleite E, Soria-Verdugo A. Experimental evaluation of the convection heat transfer coefficient of large particles moving freely in a fluidized bed reactor. Int J Heat Mass Transf 2020;153:119612. https://doi.org/10.1016/j.ijheatmasstransfer.2020.119612.
[35] Fattahi M, Hosseini SH, Ahmadi G, Parvareh A. Numerical simulation of heat transfer coefficient around different immersed bodies in a fluidized bed containing Geldart B particles. Int J Heat Mass Transf Oct. 2019;141:353–66. https://doi.org/10.1016/j.ijheatmasstransfer.2019.06.058.
[36] W. Prins, "Fluidized Bed Combustion of a Single Carbon Particle," 1987.
[37] Chao J, Lu J, Yang H, Zhang M, Liu Q. Experimental study on the heat transfer coefficient between a freely moving sphere and a fluidized bed of small particles. Int J Heat Mass Transf 2015;80:115–25. https://doi.org/10.1016/j.ijheatmasstransfer.2014.08.049.
[38] Gunn DJ. Transfer of heat or mass to particles in fixed and fluidised beds. Int J Heat Mass Transf 1978;21(4):467–76. https://doi.org/10.1016/0017-9310(78)90080-7.
[39] Agarwal PK. Transport phenomena in multi-particle systems-II. Particle-fluid heat and mass transfer. Chem Eng Sci 1988;43(9):2501–10. https://doi.org/10.1016/0009-2509(88)85184-4.
[40] Collier AR, Hayhurst AN, Richardson JL, Scott SA. The heat transfer coefficient between a particle and a bed (packed or fluidised) of much larger particles. Chem Eng Sci Nov. 2004;59(21):4613–20. https://doi.org/10.1016/J.CES.2004.07.029.
[41] Scott SA, Davidson JF, Dennis JS, Hayhurst AN. Heat Transfer to a Single Sphere Immersed in Beds of Particles Supplied by Gas at Rates above and below Minimum Fluidization. Ind Eng Chem Res 2004;43(18):5632–44.
[42] Li T, Gopalakrishnan P, Garg R, Shahnam M. CFD–DEM study of effect of bed thickness for bubbling fluidized beds. Particuology Oct. 2012;10(5):532–41. https://doi.org/10.1016/j.partic.2012.02.006.
[43] Grace J, Bi X, Ellis N, editors. Essentials of Fluidization Technology. Wiley; 2020.
[44] Glicksman LR, Hyre MR, Farrell PA. Dynamic similarity in fluidization. Int J Multiph Flow 1994;20(Suppl. 1):331–86. https://doi.org/10.1016/0301-9322(94)90077-9.
[45] Glicksman LR. Scaling relationships for fluidized beds. Chem Eng Sci 1984;39(9):1373–9. https://doi.org/10.1016/0009-2509(84)80070-6.
[46] Gaston KR, Jarvis MW, Pepiot P, Smith KM, Frederick WJ, Nimlos MR. Biomass Pyrolysis and Gasification of Varying Particle Sizes in a Fluidized-Bed Reactor 2011;25(8):3747–57.
[47] R. P. Ma, R. M. Felder, and J. K. Ferrell, "Modeling a pilot-scale fluidized bed coal gasification reactor," vol. 19, pp. 265–290, 1988.
[48] G. Ruoppolo, A. Cante, R. Chirone, F. Miccio, and V. Stanzione, "Set up of a pilot scale catalytic fluidized bed reactor for biomass gasification," *Chem Eng Trans*, vol. 17, no. October 2014, pp. 13–18, 2009, doi: 10.3303/CET0917003.
[49] Parrillo F, Ardolino F, Calì G, Marotto D, Pettinau A, Arena U. Fluidized bed gasification of eucalyptus chips: Axial profiles of syngas composition in a pilot scale reactor. Energy 2021;219:119604. https://doi.org/10.1016/j.energy.2020.119604.
[50] E. Kuznetsova, R. Motenko, and S. Willy Danielsen, "Thermal properties of volcanic ash and pumice," vol. 4, no. May 2015, pp. 12–15, 2013, doi: 10.13140/RG.2.1.1916.8165.

[51] Patti A, Acierno D. Thermal Conductivity of Polypropylene-Based Materials. In: Wang W, Zeng Y, editors. Polypropylene - Polymerization and Characterization of Mechanical and Thermal Properties. IntechOpen; 2020.

[52] Chao J, Lu J, Yang H, Zhang M, Liu Q. Experimental study on the heat transfer coefficient between a freely moving sphere and a fluidized bed of small particles. Int J Heat Mass Transf 2015;80:115–25. https://doi.org/10.1016/j.ijheatmasstransfer.2014.08.049.

[53] Bruni G, Solimene R, Marzocchella A, Salatino P, Yates JG, Lettieri P, et al. Self-segregation of high-volatile fuel particles during devolatilization in a fluidized bed reactor. Powder Technol 2002;128(1):11–21.

[54] MacDONALD CAROLYNA, editor. An Introduction to X-Ray Physics, Optics, and Applications. Princeton University Press; 2017.

[55] M. Vollmer K.-P. Möllmann Infrared Thermal Imaging 2018 Wiley-VCH Verlag GmbH & Co. KGaA Weinheim, Germany 10.1002/9783527693306.

[56] Wolfesberger-Schwabl U, Aigner I, Hofbauer H. Mechanism of Tar Generation during Fluidized Bed Gasification and Low Temperature Pyrolysis. Ind Eng Chem Res 2012;51(40):13001–7.

[57] Arena U. Process and technological aspects of municipal solid waste gasification. A review. Waste Manag 2012;32(4):625–39. https://doi.org/10.1016/j.wasman.2011.09.025.

[58] Sette E, Pallarès D, Johnsson F. Experimental quantification of lateral mixing of fuels in fluid-dynamically down-scaled bubbling fluidized beds. Appl Energy 2014; 136:671–81.

[59] Garcia-Gutierrez LM, Soria-Verdugo A, Ruiz-Rivas U. Optimization of the feeding ports location in a fluidized bed combustor based on Monte Carlo simulations of fuel particles motion. Fuel 2015;141:82–92. https://doi.org/10.1016/j.fuel.2014.10.027.

[60] G. M. Rios and H. Gibert, "Heat Transfer Between Gas Fluidized Bed and Big Bodies; Analysis and Explanation of Big Body Mobility Effect," in *Fourth International Engineering Foundation Conference on Fluidisation*, 1983, pp. 363–371.

[61] Prins W, Maziarka P, De Smedt J, Ronsse F, Harmsen J, Van Swaaij WV. Heat transfer from an immersed fixed silver sphere to a gas fluidized bed of very small particles. Therm Sci 2019;23:S1425–33. https://doi.org/10.2298/TSCI180928175P.

[62] Garcia-Gutierrez LM, Hernández-Jiménez F, Cano-Pleite E, Soria-Verdugo A. Experimental evaluation of the convection heat transfer coefficient of large particles moving freely in a fluidized bed reactor. Int J Heat Mass Transf 2020;153: 119612. https://doi.org/10.1016/j.ijheatmasstransfer.2020.119612.

[63] Martin JS. Botterill, *Fluid-bed heat transfer : gas-fluidized bed behaviour and its influence on bed thermal properties.* London: Academic Press; 1975.

[64] Parmar MS, Hayhurst AN. The heat transfer coefficient for a freely moving sphere in a bubbling fluidised bed. Chem Eng Sci 2002;57(17):3485–94. https://doi.org/10.1016/S0009-2509(02)00259-2.

[65] Ranz WE, Marshall WR. Evaporation from drops - Part 1. Chem Eng Prog 1952;48: 141–8.

[66] N. Wakao, *Heat and mass transfer in packed beds.* in Topics in chemical engineering v. 1. New York ; Gordon and Breach Science, 1982.

[67] Scott SA, Davidson JF, Dennis JS, Hayhurst AN. Heat Transfer to a Single Sphere Immersed in Beds of Particles Supplied by Gas at Rates above and below Minimum Fluidization. Ind Eng Chem Res 2004;43(18):5632–44.

[68] Collier AR, Hayhurst AN, Richardson JL, Scott SA. The heat transfer coefficient between a particle and a bed (packed or fluidised) of much larger particles. Chem Eng Sci Nov. 2004;59(21):4613–20. https://doi.org/10.1016/J.CES.2004.07.029.